

Northumbria Research Link

Citation: Stern, A. A., Holland, D. M., Holland, P. R., Jenkins, Adrian and Sommeria, J. (2014) The effect of geometry on ice shelf ocean cavity ventilation: a laboratory experiment. *Experiments in Fluids*, 55 (5). p. 1719. ISSN 0723-4864

Published by: Springer

URL: <https://doi.org/10.1007/s00348-014-1719-3> <<https://doi.org/10.1007/s00348-014-1719-3>>

This version was downloaded from Northumbria Research Link:
<http://nrl.northumbria.ac.uk/id/eprint/42655/>

Northumbria University has developed Northumbria Research Link (NRL) to enable users to access the University's research output. Copyright © and moral rights for items on NRL are retained by the individual author(s) and/or other copyright owners. Single copies of full items can be reproduced, displayed or performed, and given to third parties in any format or medium for personal research or study, educational, or not-for-profit purposes without prior permission or charge, provided the authors, title and full bibliographic details are given, as well as a hyperlink and/or URL to the original metadata page. The content must not be changed in any way. Full items must not be sold commercially in any format or medium without formal permission of the copyright holder. The full policy is available online: <http://nrl.northumbria.ac.uk/policies.html>

This document may differ from the final, published version of the research and has been made available online in accordance with publisher policies. To read and/or cite from the published version of the research, please visit the publisher's website (a subscription may be required.)



**Northumbria
University**
NEWCASTLE



UniversityLibrary

The effect of geometry on ice-shelf ocean cavity ventilation: a laboratory experiment

A.A. Stern · D.M. Holland · P.R. Holland · A. Jenkins · J. Sommeria

Received: date / Accepted: date

Abstract A laboratory experiment is constructed to simulate the density driven circulation under an idealized Antarctic ice shelf and to investigate the flux of dense and fresh water in and out of the ice shelf cavity. Our results confirm that the ice front can act as a dynamic barrier that partially inhibits fluid from entering or exiting the ice shelf cavity, away from two wall-trapped boundary currents. This barrier results in a density jump across the ice front and in the creation of a zonal current which runs parallel to the ice front. However despite the barrier imposed by the ice front, there is still a significant amount of exchange of water in and out of the cavity. This exchange takes place through two dense and fresh gravity plumes which are constrained to flow along the sides of the domain by the Coriolis force. The flux through the gravity plumes and strength of the dynamic barrier are shown to be sensitive to changes in the ice shelf geometry and changes in the buoyancy fluxes which drive the flow.

A.A. Stern
Courant Institute of Mathematical Science, New York University, New York, 10012, USA
Tel.: +1-858-353-7179
E-mail: alon@cims.nyu.edu

D.M. Holland
Courant Institute of Mathematical Science, New York University, New York, 10012, USA

P.R. Holland
British Antarctic Survey, High Cross, Madingley Road, Cambridge CB3 0ET, United Kingdom

A. Jenkins
British Antarctic Survey, High Cross, Madingley Road, Cambridge CB3 0ET, United Kingdom

J. Sommeria
Institut de Mecanique, Universite de Grenoble, B.P. 53X, 38041 Grenoble Cedex, France

Keywords ice-shelf · laboratory experiment · gravity plume

1 Introduction

The Greenland and Antarctic ice sheets are comprised of many separate ice streams, fast-flowing rivers of ice that flow downhill under gravity. Where these ice streams come into contact with the oceans, they either fracture and calve icebergs, or they form ice shelves, large floating glaciers that can be several kilometers thick and several hundreds of kilometers wide.

The dynamics of the water within ice shelf cavities and the flux of dense water in and out of the ice shelf cavities, has a strong influence on the calving and melting rates of the ice shelves. However, the large quantity of ice above the cavities has made observational measurements extremely difficult and as a result, there exists relatively little data about the circulation within the cavities. In addition to this, the sloping and melting upper boundary above the cavity has a strong effect on the dynamics of the flow within the cavity and makes the dynamics distinct from all other ocean flows.

Nevertheless, in the past 30 years a small body of observational measurements under the Antarctic ice shelves has begun to be created (e.g.: [39] [33] [34] [40] [18] [28]) and a general picture of dominant dynamical processes which take place within the ice shelf cavities has begun to emerge. The first one-dimensional models to describe ocean-ice interactions within the Antarctic ice shelf cavities were put forward by MacAyeal [4] [5] and Jenkins [26] and later extended to a 2-D model by Holland & Feltham [20]. This model can be summarized as follows (Figure 1). The cold Antarctic winter conditions cause the surface water at the ice front to freeze. The salt rejected during freezing mixes with the cold ambient surface water to form High Salinity Shelf Water (HSSW). The dense HSSW sinks to the bottom of the water column and flows down into the ice shelf cavity towards the grounding line.

Since the freezing point of sea water decreases with depth, the temperature of the HSSW, which was formed at the surface, is warmer than the freezing point of sea water at the grounding line. When the HSSW comes into contact with the ice at the grounding line it causes the ice to melt, releasing cold fresh melt water into the ice cavity. The melt water and HSSW mix to form a plume of buoyant Ice Shelf Water (ISW), which rises up along the shelf base.

As it rises, the ISW becomes super-cooled and begins to form frazil ice. Much of this frazil ice deposits itself on the underside of the ice shelf, where it is known as marine ice. The dynamics of the upward moving plume is further complicated by the fact that it is subject to the Coriolis force, and that it entrains ambient water as it rises. Eventually the ISW may become neutrally buoyant and leave the ice shelf base. Some of this ISW makes it to the ice

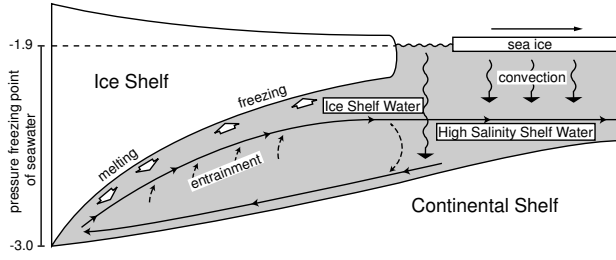


Fig. 1 Schematic diagram of processes beneath an idealized ice shelf.

front and becomes an important factor in processes taking place at the ice front [40], including the formation of Antarctic deep and bottom water. The entire process described in the previous three paragraphs is known as the ice pump.

The energy budget for the ice pump involves complicated thermodynamic interactions, lattice ice energy and the non-linear equation of state of sea water [37] [21] [19]. However, at the most basic level, the ice pump process can be seen as being a buoyancy driven circulation forced by the injection of dense water (HSSW) at the ocean surface, and the injection of fresher water (ISW) at depth, which effectively injects potential energy into the system. By neglecting the temperature variations and thermodynamics, as we shall in our study, one can focus on how these buoyancy sources, the structure of the bottom topography and the structure of the ice shelf determine the flow.

The dynamical effects of the ice shelf topography were studied by Determan and Gerdes [11] and Grosfeld et al [17]. These studies used numerical models to demonstrate that the ice front has a major effect on the flow, and essentially blocks waters from the open ocean from entering the cavity as a result of a potential vorticity constraint. More recent work has shown that this blocking effect is not as powerful as previously supposed [22] and depends on the stratification of the water arriving at the ice front [33]. Recent work has shown that eddies are able to intrude into the ice shelf cavity [2]. Furthermore, boundary currents are able to enter and exit the ice shelf cavity quite freely and are able to transport a large volume of water into the cavity [22].

The boundary currents which run into the ice shelf cavity are examples of rotating gravity currents. Rotating gravity currents on a slope have been studied at length both experimentally and theoretically [6] [9] [31] [49] [29] [8]. The problem of rotating density currents along a solid lateral boundary has also been studied [15] [16] [45]. These large scale topographically steered gravity currents are important since they control a large proportion of the flux into the ice shelf cavity, and can also affect the properties of the ambient fluid in the ice shelf cavity via entrainment [47]. However, it is unknown how these

gravity currents respond to the presence of an ice shelf, which acts as an upper boundary.

In nature, bottom and ice shelf topographies are important in steering the dense water into the ice shelf cavity, and fresh water out of the ice shelf cavity. Observations indicate that the main pathways for HSSW are through depression in the ocean bottom and along land boundaries [41] [36]. Similarly, buoyant ice shelf water leaving the ice shelf cavity is steered by the bathymetry and by the ice shelf geometry [20]. The ice shelf topography also plays a role in directing ocean jets outside of the ice shelf cavity which run along the ice front [43] [12]. The role that these topographically steered jets play in the exchange of water into and out of the cavity is still unknown. In real-world ice shelves, easterly winds at the ice front are involved in driving the jet, which further complicates the dynamics.

In this study, a laboratory experiment is created to simulate the density driven currents involved in the ice pump. The first aim of the experiment was to observe how water passes into and out of the ice shelf cavity and estimate the flux of dense water which moves into the cavity as a gravity plume along the lateral boundary. Secondly, the experiment aimed to determine how the flux of dense water into the cavity, the flux of fresh water out of the cavity, the circulation inside the cavity, and the structure of the gravity plumes moving into and out of the cavity, are affected by varying the buoyancy fluxes injected into the system, and varying the geometry of the ice shelf cavity.

In the experiment described below, the flow was visualized using Particle Image Velocimetry (PIV) [1] and Laser Induced Florescence (LIF) [25]. Recent advancements in flow visualization in laboratory experiments has meant that laboratory experiments can be used for quantitative rather than qualitative geophysical applications. However, in recent years the use of laboratory experiments to study ocean-ice interaction has not been popular. One of the purposes of this study is to present observations and lessons from a first effort obtaining quantitative data to help understand sub-ice shelf circulation.

Section 2 explains the experimental setup, measurement methods and calibration process. The results of the experiments are outlined in Section 3. Section 4 contains a brief discussion of the results. Section 5 contains a some concluding remarks.

2 Experimental setup and data collection

The experiment described below was performed on a rotating platform in the Coriolis laboratory, in Grenoble, France. In this section we explain the experimental setup, the different types of experimental runs, and comment on the

data collected.

2.1 Experimental Setup

The experimental setup was motivated by the descriptions of the ‘ice pump’ described in the introduction [4] [26] [20]. Figure 2, which shows our experimental setup, can be compared to Fig. 1 which is a schematic of the process we were trying to mimic. The upper panel in Fig. 2 shows a side view of our experimental domain. The plan view of the experiment is shown in the lower panel of Fig. 2. The base of the experimental domain consisted of the cavity continental slope with a slope of 0.1 and a level continental shelf. These are shown from left to right in the upper panel in Fig. 2. An ice shelf was created using Plexiglas and was positioned above the sloping bottom as shown in Fig. 2. Between the ice shelf and slope there was a region which we refer to as the ice shelf cavity.

The entire domain shown in Fig. 2 was placed inside the large 13m rotating platform which rotated counter-clockwise with a period of 60 seconds. The Grenoble turntable was only able to turn in the counter-clockwise direction, so the experiment simulated a northern hemisphere ice shelf (i.e. $f > 0$). Since the experiment was meant to model the Antarctic ice shelves, we will refer to the left most side of Fig. 2 as the southern most point (we are free to make this choice as we have constant rotation everywhere in the domain). The other directions are named accordingly. The x, y and z axes are defined using the standard direction convention: the positive direction on the y-axis is north, the positive direction on the x-axis is east, and the positive direction on the z-axis is up.

At the southern end of the ice shelf cavity, we constructed a barrier, which we refer to as the continent. The point where the ice shelf base meets the continent is referred to as the grounding line. The height of the grounding line is denoted h_g . At the northern end of the experimental setup, there was a barrier to keep the fluid inside the experimental domain. The domain was 400cm from north to south, 200cm from east to west and 56cm from top to bottom.

Two water masses were used in the experiment: Fresh water with density of $1000 \frac{\text{kg}}{\text{m}^3}$ and dense water with a density of $1004 \frac{\text{kg}}{\text{m}^3}$. These densities were chosen for the dense and fresh water since the difference between the densest and freshest waters found under Antarctic ice shelves is $\sim 4 \frac{\text{kg}}{\text{m}^3}$. The dense water was seeded with Rhodamine dye, which was used to measure the water density during the experiments (see section 2.4). Both water masses were seeded with micrometer sized particles which were used to calculate the velocity fields during the experiment (see section 2.4). At the beginning of the experiment,

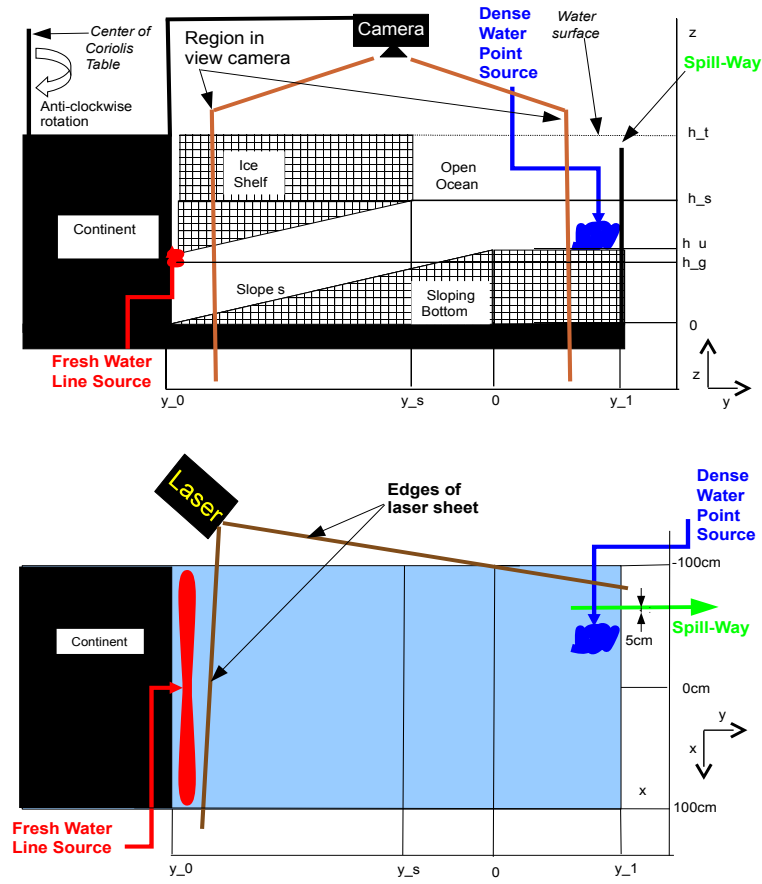


Fig. 2 The experimental setup for our experiment. The upper panel shows the side view of the experiment. The lower panel shows the plan view of the experiment. The red and blue marks indicate the position of the fresh and dense water sources, respectively. The y -axis indicates latitude, the x -axis indicates the zonal direction. The positive y direction points north and the positive x -axis points east.

the entire domain was filled with mixture of the fresh and dense water. The experimental results were insensitive to the ratio of this initial mixture since measurements were only made after the system had reached equilibrium.

A fresh water line source was placed along the grounding line. When this source was switched on, it created a plume of buoyant fresh water which rose up along the ice shelf base. This plume represented the Ice Shelf Water (ISW) discussed in the previous section. The water injected at the fresh source was injected vigorously creating some mixing. The fresh water source contained some bubbles that we were unable to prevent during the experiment, but these did not materially affect our results. Just outside of the ice shelf cavity, we placed a dense water point source near the north-west corner of the domain. The dense water injected here formed a gravity current which rolled down the slope and into the cavity. This dense water represented the High Salinity Shelf Water (HSSW) discussed in the previous section. A sponge was used to limit the mixing and bubbles caused by injecting the dense water. A point source was used for the the dense water injection since the production of HSSW is often a localized process [36] [2]. A line source was used for the fresh water source since melting occurs all along the grounding line.

At the north-west corner of the domain, there was an opening which we refer to as the spill-way. Water was allowed to drain out of the experimental domain through the spill-way. In this way, the total amount of water in the domain remained fixed.

The experiment was spun-up for two hours to be in solid body rotation before the dense and fresh sources were turned on. After the dense and fresh sources were turned on, there was an unsteady period where the system adjusted to a new equilibrium. All measurements and analysis were performed after this adjustment had been completed and the system was in a statistically steady state. The waiting time after the dense and fresh sources were turned on, was approximately one hour, which is greater than the flushing time for the system, T_f , and the spin-up time, T_s (see Section 2.2.1). Measurements of the density driven circulation were observed using a camera positioned above the experimental domain. In the different experimental runs measurements were taken for between 4000 and 10000 seconds.

Three tests were performed to explore the effect of ice geometry and buoyancy sources on the ice shelf circulation:

- **Thickness Investigation:** The thickness of the ice shelf cavity was varied, while the slope of the ice shelf, and the buoyancy sources, were kept constant.
- **Gradient Investigation:** The gradient of the ice shelf was varied while the buoyancy sources were kept constant.

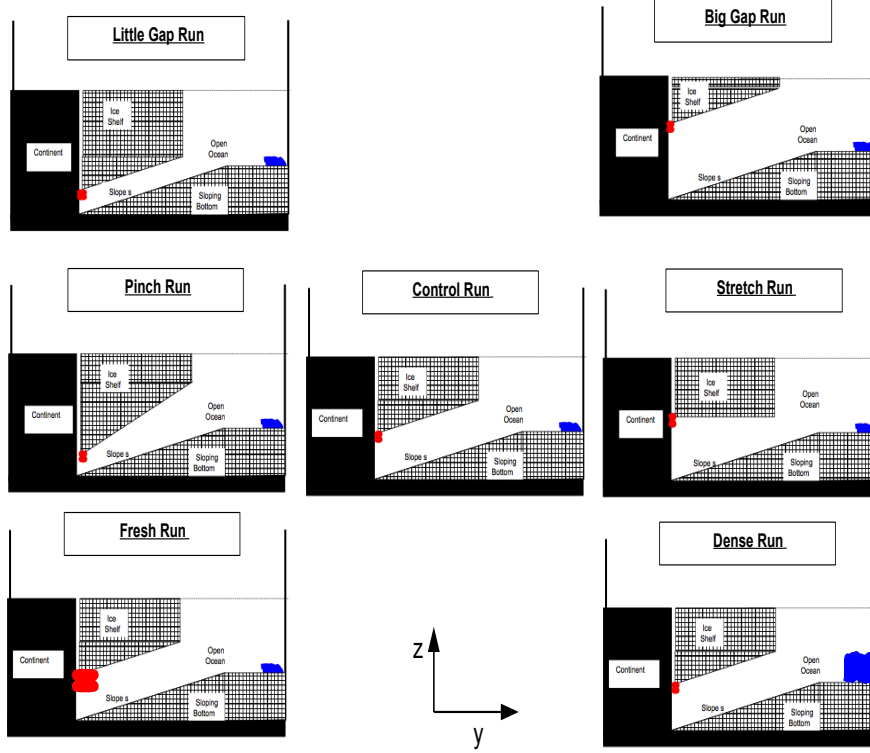


Fig. 3 Summary of seven different experiments runs performed. The seven experimental runs are divided into three experiments. All three experiments used the same Control Run, which is positioned in the center. The top row shows Thickness Investigation where the ice shelf cavity thickness was varied. Row two shows Gradient Investigation where the slope of the ice shelf was varied. Row three shows Buoyancy Investigation, where the control geometry was used, but the fluxes of the dense and fresh water sources were varied.

Experiment	Dense Flow Rate	Fresh Flow Rate	h_g (cm)	h_s (cm)
Control Run	20.05 l/min	20.00 l/min	20.0	41.3
Fresh Run	10.04 l/min	30.00 l/min	20.0	41.3
Dense Run	30.63 l/min	10.00 l/min	20.0	41.3
Pinch Run	19.93 l/min	21.67 l/min	9.0	43.8
Stretch Run	20.30 l/min	21.67 l/min	30.0	36.3
Big Gap Run	20.00 l/min	20.00 l/min	29.7	51.0
Little Gap Run	20.00 l/min	20.00 l/min	10.0	31.3

Table 1 Parameters used in the experimental runs

- **Buoyancy Investigation:** The buoyancy sources were varied, while the ice shelf geometry was kept constant.

In the rest of the paper, we refer to these three investigations as the Thickness Investigation, Gradient Investigation and Buoyancy Investigation. The term *experimental runs*, is used throughout the rest of the paper to refer to individual simulations which made up these three *investigations*. Each investigation consisted of three experimental runs. The number of experimental runs was limited by the time taken to run an experiment and the complexity of the experimental setup. The same Control Run was used for all three investigations meaning that in total, seven different experimental runs were performed.

Figure 3 shows a schematic of the experimental runs performed. The three investigations are shown from left to right in rows one, two and three of Fig. 3, with the Control Run in the center. The various experimental runs are named in Fig. 3. These names are used throughout the discussion below. Different geometries were achieved by changing h_g and h_s . All experimental runs used $y_0 = -250\text{cm}$, $y_1 = 169\text{cm}$, $y_s = -38\text{cm}$, $h_u = 25\text{cm}$, and $h_t = 56\text{cm}$. Table 1 has a list of the experimental parameters used in the various experimental runs.

2.2 Non-dimensional numbers:

2.2.1 Non-dimensional numbers showing dynamic similarity:

The large Coriolis facility was used rather than a smaller rotating platform as the large experimental domain meant that we were able to better resolve the boundary currents in the experiment. The largeness of experimental domain also allowed us to achieve non-dimensional numbers which were more similar to the real world.

The Rossby number of our system was $R_0 = \frac{U}{fL} = \frac{10^{-2}}{0.2 \times 1} = \frac{1}{20}$. Here we use the fact that $f = \frac{4\pi}{T} = \frac{4\pi}{60} \approx 0.2$. We use $L=1\text{m}$, which half of the width of the domain and $U = 10^{-2}\text{m/s}$, which was a typical velocity observed in the experiments. The real-world Rossby number can be estimated as $R_{ocean} = \frac{U}{fL} \approx \frac{10^{-1}}{10^{-4} \times 10^5} = 10^{-2}$ where the estimate of U comes from [39]. The smallness of the Rossby number in both cases mean that the system was likely to be close to geostrophic balance.

Since we were using a large tank, we were able to achieve a small aspect ratio $\alpha_0 = \frac{H}{L} \approx \frac{0.5\text{m}}{4\text{m}} \approx 10^{-1}$. The length of the tank was 4m. The aspect ratio of the real-world ice cavities is $\alpha_{ocean} \approx \frac{10^3\text{m}}{10^5\text{m}} = 10^{-2}$. While our aspect ratio is an order of magnitude larger than that of the ocean, the both systems are strongly influenced by the smallness of their aspect ratio.

The frictional Ekman layer thickness scales like $\delta = \sqrt{\frac{\nu}{f}}$. Using the viscosity of water $\nu \approx 10^{-6} \text{m}^2 \text{s}^{-1}$, we estimate a molecular Ekman layer thickness of $\delta_{mol} = \sqrt{\frac{\nu}{f}} \approx \sqrt{\frac{10^{-6}}{\frac{1}{5}}} = 2.2 \times 10^{-3} \text{m} = 2.2 \text{mm}$. This provides a lower bound of the Ekman layer thickness. To get an upper bound on the Ekman layer thickness, we use a typical Eddy viscosity found in the ocean, $\nu = 10^{-2}$. This gives us $\delta_{tur} = \sqrt{\frac{\nu}{f}} \approx \sqrt{\frac{10^{-2}}{\frac{1}{5}}} = 22 \text{cm}$. However, since our system was likely to be much less turbulent than the ocean, it is probable that the eddy viscosity will be an order of magnitude or more smaller, resulting in an Ekman layer thickness, δ , between 1cm and 10cm, although this is hard to predict a-priori. In the experimental results shown below, the Ekman boundary layer can not be seen. This is especially apparent in the dense and fresh plumes where the fastest speeds are close to the lower and upper boundaries, respectively. This implies that the Ekman layer thickness is likely to be smaller than 2cm, the resolution of the velocity measurements.

The Reynolds number in the experiment is $Re = \frac{UL}{\nu} = \frac{10^{-2} * 1}{10^{-6}} = 10^4$. Since the transition to turbulence typically occurs for $2300 < Re < 4000$ (in a pipe flow) [23], the fluid in our experiment was likely to have been turbulent. While the Reynolds number is smaller than typical Reynolds numbers found in the ocean, it is comparable to Reynolds numbers used in numerical models. The Froude number for the gravity plumes in the experiment is $F = \frac{U}{\sqrt{g'H}} = \frac{10^{-2}}{\sqrt{10^{-2} * 10^{-1}}} \sim 0.3$, which is slightly subcritical.

The spin-up time for a rotating tank is $T = \sqrt{\frac{L^2}{\nu}} \Omega$ [14]. In our experiment the spin-up time is estimated as $T = \sqrt{\frac{L^2}{\nu}} \Omega = \sqrt{\frac{1 \text{m}^2}{10^{-6} \text{m}^2 \text{s}^{-1} \frac{2\pi}{60}}} \sim 10^{\frac{7}{2}} \text{s} \sim 3000 \text{s}$. The experiments were allowed to spin up for two hours to reach solid body rotation before the flow was turned on. The experimental domain contained $\sim 2 \text{m}^3$ of water. The combined flux of the dense and fresh water sources were 40 liters per minutes ($\sim 0.66 \times 10^{-3} \frac{\text{m}^3}{\text{s}}$). This meant that the flushing time for the system was $T_f \sim 3000 \text{s}$.

2.2.2 Non-dimensional parameters varied in experiments:

The changes in geometry and buoyancy used in the three investigations can be described by three non-dimensional numbers: G_t , G_s and G_b . These are described below:

We define G_t as the the ratio of the thickness of the water column inside and outside the ice shelf cavity at the ice front. Since the height of the ocean

floor at the ice front is $h_u - |y_s|s$, we define

$$G_t = \frac{h_s - (h_u - |y_s|s)}{h_t - (h_u - |y_s|s)} \quad (1)$$

Here s is the slope of the ocean bottom. G_t gives a measure of the change of water column thickness which occurs as a column of fluid moves across the ice front.

G_s is defined to be the average meridional gradient of the ice cavity thickness. In our setup, G_s is given by

$$G_s = \frac{(h_g - 0) - (h_s - (h_u - |y_s|s))}{|y_0 - y_s|} \quad (2)$$

G_s gives a measure of how the cavity water column thickness changes as a column of fluid moves from the grounding line to the ice front.

G_b is defined as the ratio of the mass flux anomaly caused by injecting dense and fresh water injected into the system.

$$G_b = \frac{\Delta M_d}{\Delta M_d} \quad (3)$$

If the ambient water in the system has a density of ρ_a , the dense water has a density of ρ_d , and the fresh water has a density of ρ_f , then the mass flux anomalies are give by

$$\Delta M_d = (\rho_d - \rho_a)Q_d \quad (4)$$

$$\Delta M_f = (\rho_a - \rho_f)Q_f \quad (5)$$

Here Q_d and Q_f are the fluxes of water injected at the dense and fresh source, respectively. The density of the dense and fresh waters injected into the system were, $\rho_d = 1004 \frac{\text{kg}}{\text{m}^3}$ and $\rho_f = 1000 \frac{\text{kg}}{\text{m}^3}$. We set $\rho_a = \frac{(\rho_d + \rho_f)}{2} = 1002 \frac{\text{kg}}{\text{m}^3}$.

In the Control Run we used $G_t = 0.58$, $G_s = 0.00$ and $G_b = 1.0$. Values were picked in order to make the control run analogous to the Ross Ice Shelf. The average ice draft of Ross Ice Shelf at the ice front is $\sim 300\text{m}$, while the continental shelf depth is $\sim 700\text{m}$ below sea level [10]. This gives $G_t \sim \frac{400\text{m}}{700\text{m}} \sim 0.57$. At 180°W , the Ross Ice Shelf cavity thickness changes by 300m over a distance of 300km between 79°S and 82°S [10]. This implies $G_s \sim \frac{1}{1000}$.

To calculate G_b we use the freshwater flux in the Ross Sea caused by sea ice production, evaporation, precipitation and the basal melt beneath the Ross Ice Shelf. Assmann et al (2003) estimated the total flux of fresh water from basal melt beneath the Ross Ice Shelf to be 5.3mSv [3]. The total fresh water flux on the Ross Sea continental shelf (excluding the contribution of melt water from under the ice shelf) was estimated to be -26.6mSv . Here $1\text{mSv} = 10^3 \text{m}^3 \text{s}^{-1}$.

Taking the ratio, this gives $G_b \sim 5$. However, a large portion of the dense water created in the Ross Sea is exported off the continental shelf and does not influence the dynamics under the ice shelf [42] [13]. Because of this uncertainty in the total amount of fresh water extraction which affects the ice shelf dynamics, we note that $G_b \sim O(1)$, and used $G_b = 1$ in our Control Run. The Dense Run and Fresh Run are used to examine the effect of changes in G_b on the circulation beneath the ice shelf.

The values of G_t , G_s and G_b used in the three different investigations are shown in Table 2. Values of G_t , G_s and G_b were varied in order to examine the sensitivity of the circulation to changes in these parameters. These experiments are motivated by the fact that paleoclimate records show that the geometry and basal melt of the Ross Ice Shelf has changed significantly in the past [7]. We are interested in how the circulation beneath the Ross Ice Shelf might have responded to such changes. Furthermore, these experiments are also of interest in comparing different ice shelves around Antarctica, which have differing geometries and buoyancy fluxes. The Ronne-Filchner Ice Shelf, for example, has a large ice draft at the ice front and therefore has a smaller value for G_t , while the ice front draft of the McMurdo Ice Shelf is only 20m, and hence $G_t \sim 1$ [46]. Pine Island Glacier has a large value for G_s since it has an ice shelf which is many times steeper than the Ross Ice Shelf, resulting in a large change of cavity thickness over a shorter distance. G_s can also be negative locally when there is steep bottom topography. The large flux of ISW associated with rapidly melting ice shelves likely results in a small value of G_b . Changing values of G_b could be relevant to future climate change scenarios.

2.3 Data collected during the experiments

A camera was placed above the experimental domain, and a laser was placed south-west of the domain (see Fig. 2). The walls of the domain were constructed using plexiglas to allow the laser light to pass through. The laser created a horizontal plane of light, which allowed the camera to take pictures of the fluid illuminated by the laser. A mirror was placed on a carriage which could move up and down, and direct the laser light to different levels so that we were able to get images in 23 different horizontal planes. The camera position remained fixed 5m above the experimental domain, rotating with the table. The camera was sufficiently far from the domain that the camera focus was not significantly affected by moving the laser sheet. At each level, 3 images were taken at a frequency of 3Hz. The images at different heights were taken 3 seconds apart. This meant that the images at every horizontal plane had a time separation of 69 seconds. The size of the region in the view of the camera was 226cm in the north-south direction and 200cm in the east-west direction. The entire width of the domain (including the plumes on both sides of the

Thickness Investigation			
Experimental Run	G_t	G_s	G_b
Little Gap Run	0.29	0.00	1.0
Control Run	0.58	0.00	1.0
Big Gap Run	0.86	0.00	1.0

Gradient Investigation			
Experimental Run	G_t	G_s	G_b
Pinch Run	0.65	-0.06	0.9
Control Run	0.58	0.00	1.0
Stretch Run	0.43	0.07	0.9

Buoyancy Investigation			
Experimental Run	G_t	G_s	G_b
Fresh Run	0.58	0.00	0.3
Control Run	0.58	0.00	1.0
Dense Run	0.58	0.00	3.1

Table 2 Non-dimensional parameters used in the experimental runs. The experimental runs have been grouped into three groups corresponding to the Thickness Investigation, the Gradient Investigation and the Buoyancy Investigation. The same control run was used for all three investigations.

domain) was in the sight of the camera, while just over half of the length of the domain (from north to south) was captured by the cameras. The fresh and dense sources were not in the field of view.

The fluid in the experiment was seeded with micrometer sized particles and the dense water injected at the dense source was mixed with a known concentration of Rhodamine dye. The Rhodamine dye and the seeded particles were illuminated by the laser and showed up in the images captured by the camera. These images were used to perform Particle Image Velocimetry (PIV), which involves finding the peak correlations between consecutive images in order to calculate horizontal velocity fields. Three images were used to calculate each velocity field. This was done by finding the peak correlation of each image with the other two, and averaging the three velocity fields. This technique helped us improve the quality of the velocity fields calculated. Multiple rounds of correlation were performed with velocity estimates from the previous round of correlations being used to refine the search parameters for subsequent correlation searches. The camera images were also used for Laser Induced Florescence (LIF), which involves using the intensity of the fluoresced light to find the concentration of Rhodamine dye in a fluid parcel, from which one can find the density of the fluid. The laser being placed on the south-west of the domain meant that the quality of the data on the side closest to the laser was better than the data on the far side. This meant that the quality of data in the dense plume was higher than the data quality in the buoyant plume.

A complex calibration process was used to convert the photographs taken during the experiments into velocity fields and concentration fields. Complications

were caused by the fact that we had to mask out the ice shelf and solid geometries during the PIV correlation procedure. The program UVMAT was used to do the correlations for the PIV (further information about UVMAT software can be found at <http://coriolis.legi.grenoble-inp.fr/spip.php?rubrique14>). The correlation percentages indicate the quality of the velocity field at a particular point. These percentages confirm that the highest quality velocity data was on the western side of the domain, near to the laser.

The procedure used for the calibration of the concentration had to account for the exponential decay of light as it passes through the rhodamine dye. The decay coefficients were calculated for each geometry separately using pictures taken with the entire domain filled with dense water (i.e. concentration of Rhodamine dye equal to 1 everywhere).

2.4 Quality of data after calibration

Figure 4 shows a typical concentration field obtained in the experiment. This example was taken from the Pinch Run, at $z = 30.5\text{cm}$. A horizontal cut is marked on the figure and the density at the cut is shown below. The dense and buoyant plumes discussed in the previous sections, can be seen along the left and right side of the figure, respectively. The velocity of the dense and buoyant plumes are shown in Box1 and Box2, where velocity is shown by the direction and size of the arrows, and the concentration is given by the color of the arrows. We define the dimensionless concentration $c = \frac{\rho - 1000}{4}$, which is the proportion of a grid box filled with Rhodamine dye. Since the Rhodamine dye is a proxy of density, c can be thought of as being normalized density, where $c = 1$ is the densest water in the domain (i.e. $\rho = 1004\text{kg m}^{-3}$) and $c = 0$ is fresh water (i.e. $\rho = 1000\text{kg m}^{-3}$).

The horizontal velocity fields have a horizontal spatial resolution of 1cm and a vertical resolution of approximately 2cm. The domain where we have data consist of 199 points in the x -direction, 226 points in the y -direction and 23 points in the z -direction (the vertical levels were not uniformly spaced). Again, the temporal resolution of the data is 69 seconds.

The accuracy of the concentration fields, c , is between 5 and 10 percent. Since the density is always in the range $1000 \frac{\text{kg}}{\text{m}^3} < \rho < 1004 \frac{\text{kg}}{\text{m}^3}$, this is equivalent to having an accuracy of between 0.2 and 0.4 kg m^{-3} in the density field. The accuracy is improved by averaging over time and space. The accuracy of the velocity field is approximately 5 percent. The major errors in the concentration field are caused by reflections of the laser off the ice front and the sloping bottom. There are also some reflections caused by bubbles, which entered the domain near via the fresh water source, and reflections off the PIV particles.

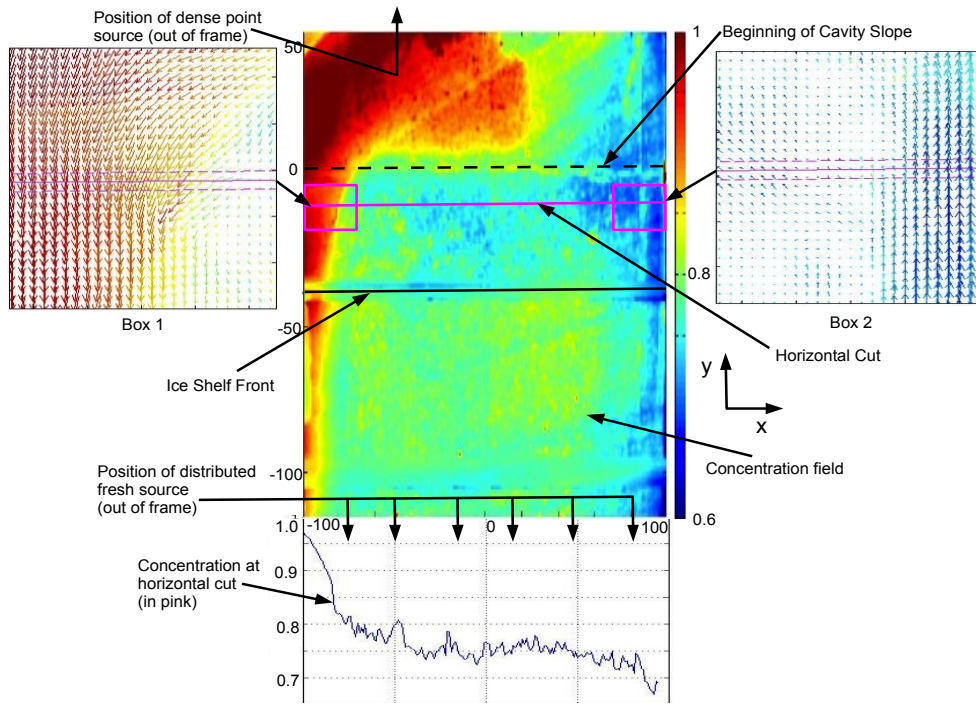


Fig. 4 A typical concentration field on the x - y plane taken from the Pinch Run, at $z = 30.5\text{cm}$. The positive y direction points north and the positive x -axis points east. The concentration of Rhodamine dye in a grid box gives us the density of the fluid. A horizontal cut is marked in pink and the concentration at the cut is shown in the graph below. The velocity of the dense and buoyant plumes are shown in Box1 and Box2, where velocity is shown by the direction and size of the arrows, and the concentration is given by the color of the arrows.

Figure 4 captures some of the main features of the flow which show up in the time-mean plots. These are discussed further in Section 3.

2.5 Further comments about the experimental setup

The experiment was performed inside a plexiglass tank with vertical walls running along the sides of the domain. This setup was preferred to axisymmetric model since in the real-world most of the large ice shelves are bounded by land on their eastern and western sides. While land boundaries on the flanks of the ice shelves are not vertical in the real world, the simplified geometry used in this experiment captures the broad features of the larger ice shelves, and allows for boundary currents to run along the sides of the domain. The presence of a northern boundary in the experimental setup gives rise to a cy-

clonic circulation offshore of the ice front, which is analogous to the westward coastal current that pervades the continental shelf offshore of Antarctic ice shelves.

The dense source was placed on the continental shelf close to the bottom of the water column. In nature the production of dense water occurs at the top of the water column. Having the dense source at the bottom of the water column meant that we could not study the convection process, however, it allowed us to focus on the the intrusion of dense water into the ice shelf cavity.

It has been observed that the injection of dense water into a rotating system, has a tendency to generate a train of traveling baroclinic vortices [31] [9] and results in an unsteady flow. This unsteady flow was observed in our experiment near the dense source. It is probable that the production of HSSW and ISW in nature is also associated with the generation of traveling baroclinic vortices, and unsteady flow, but current real-world observations are too sparse to comment further.

The laser being positioned on the western side of the domain meant that the quality of the velocity and concentration fields in the fresh plume was lower than in the dense plume (which was closer to the light source). This meant that the quality of data in the fresh plume was only good enough for qualitative analysis. This meant that we were unable to estimate the total mass and volume flux into the cavity since this calculation is sensitive to error in the flux of water through the fresh plume. In future experiments it would be preferable to position the laser differently to ensure high quality data on both boundaries.

3 Major features of the flow

In this section we present the main features of the flow observed in the experiment. We begin our analysis by looking at the time mean features of the data. As mentioned earlier, all experimental runs were allowed a spin-up time to reach solid body rotation before the dense and fresh sources were turned on. After the sources were turned on, we again waited for the system to reach a statistically steady state. All time means have been taken over the times where a statistically steady state has been achieved.

3.1 Description of results in the Control Run:

The background colors in Fig. 5 shows the time-mean, z -mean meridional velocity for the control experiment. The arrows in Fig. 5 show the time-mean,

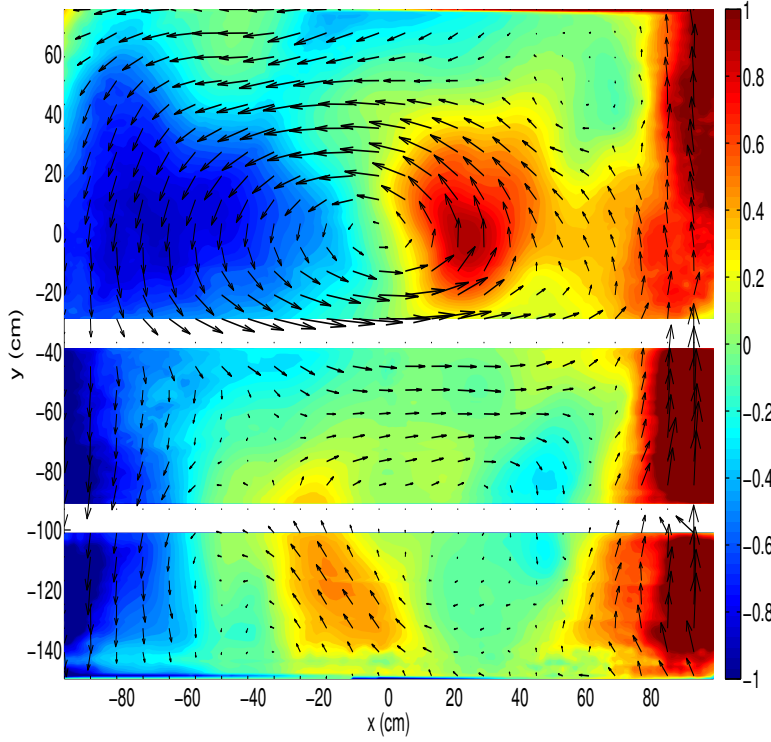


Fig. 5 The arrows show the time averaged, z -average velocity field for the Control Run. The background colors show the time averaged, z -average meridional velocity on the x - y plane. The positive y direction points north and the positive x -axis points east. The fresh and dense plumes can be seen running along the west and east sides of the cavity, respectively. The continental slope begins at $y=0$ cm and the ice front is at $y=-38$ cm.

z -mean horizontal velocity field. At latitudes $y=-38$ cm and $y=-97$ cm, the view of the camera was obstructed and we were unable to collect data. The white lines in Fig. 5 show the position these data gaps. From this figure, together with figures of the concentration fields (similar to Fig. 4), we can infer the main features of the flow: Dense water, which is injected onto the continental shelf by the dense source, diffuses into the surrounding water, remaining close to the bottom. As the dense water spreads southwards, it is acted on by the Coriolis force and veers to the west.

When the dense water reaches the beginning of the slope ($y=0$), it starts to roll down the continental slope as a gravity plume, which pushes the water even further to the west (recall we are using $f > 0$ with the ice shelf on the south of the domain). In the absence of lateral boundaries, we would expect

that the dense water would be redirected so strongly by the Coriolis force that it would eventually move parallel to the continental slope [15]. In our case, the dense fluid continues to move westward until it reaches the western wall of the domain. The dense water moves as a gravity plume along the western wall of the domain. When it reaches the ice front ($y=-38\text{cm}$), some of the dense water runs along the ice front and recirculates on the continental shelf. The remaining dense water which continues to move along the wall of the domain, enters the ice cavity and continues down the slope towards the grounding line.

The fresh water acts in a similar way but with its direction reversed. The fresh water is injected fairly vigorously and causes some mixing near the grounding line (not seen in Fig. 5). Once it is injected, the fresh water begins to flow northward because of its positive buoyancy. As it moves north, it is directed eastward by the Coriolis force and eventually reaches the eastern boundary of the domain, where it moves up the ice shelf slope as a gravity plume. Once the fresh water plume exits the ice shelf cavity, it moves quickly to the surface because of its positive buoyancy, and continues to move northward along the eastern wall. The dense and fresh plumes along the sides of the domain are seen clearly in Fig. 5.

There is relatively little motion inside the ice shelf cavity away from the boundary currents. A small clockwise gyre can be seen inside the ice shelf cavity. This gyre is much smaller than the gyre on the continental shelf, and moves in the opposite direction (i.e. against the rotation).

The vertical structure of the gravity plumes along the lateral boundaries is shown in Fig. 6. This figure shows the meridional velocity in the x - z plane at $y=-54\text{cm}$, which is a latitude inside of the ice shelf cavity. The dense and fresh plumes can be seen running into and out of the ice shelf cavity, respectively. Away from the boundary currents, the velocity of the fluid inside the ice shelf cavity is much smaller. Figure 6 is similar to Fig. 13 in Holland and Jenkins (2001) which simulated the flow under a similar idealized ice shelf using an isopycnic-coordinate ocean model [22].

The fresh water is injected vigorously by a distributed source and tends to mix with the ambient fluid. This results in the fresh plume being more homogeneous than the dense plume, and the density of the fresh plume being closer to the density of the ambient water. This could account for the steep gradient of the boundary of the fresh plume observed in Fig. 6, since decreasing the density gradient across the plume boundary requires an increased slope of the plume boundary in order for the plume to maintain the same geostrophic velocity. However the quality of the data in the fresh plume is not sufficiently high to have confidence that the asymmetry between the dense and fresh plumes, observed in Fig. 6, is a robust feature of the system.

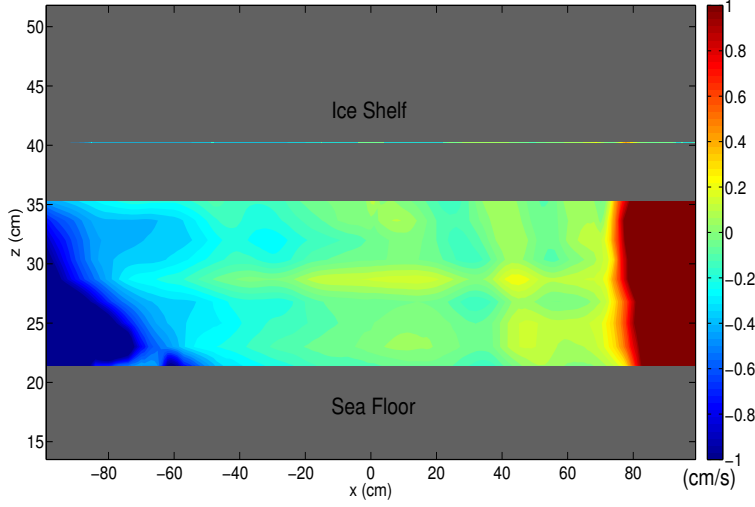


Fig. 6 The time-mean meridional velocity at $y=-54\text{cm}$, which is a latitude inside of the ice shelf cavity. The dense and fresh plumes can be seen fluxing water into and out of the ice shelf cavity, respectively.

Outside of the ice shelf cavity, on the continental shelf, the fluid that does not enter the ice shelf cavity tends to circulate in a counter-clockwise direction, producing a large gyre with positive vorticity. This gyre on the continental shelf results in a strong zonal flow along the ice front. This jet can be seen in Fig. 7 which shows the time averaged, x -mean of the zonal velocity. The jet does not penetrate far into the ice shelf cavity.

Figure 8 shows the interior concentration, C_{int} , for the Stretch Run (no concentration data was available for the Control Run). C_{int} is the average concentration of the fluid away from the eastern and western boundaries and is defined as

$$C_{int}(y, z) = \frac{1}{132} \int_{-60}^{72} c(x, y, z) dx \quad (6)$$

where c is the time-mean concentration and $x = -60$ and $x = 72$ are points which are in the interior and away from the dense and fresh boundary currents. Positions where we were unable to collect data are shown using white lines. Figure 8 shows a large density jump across the shelf break.

Since the laser used to illuminate the fluid for the LIF measurements was placed on the south-west of the domain, the shadow cast by the ice shelf was not parallel to the ice shelf front. This implies that the result shown in Fig. 8 is unlikely to be a result of calibration error, or a shadow cast by the ice shelf, but rather reflects a real density gradient across the ice front.

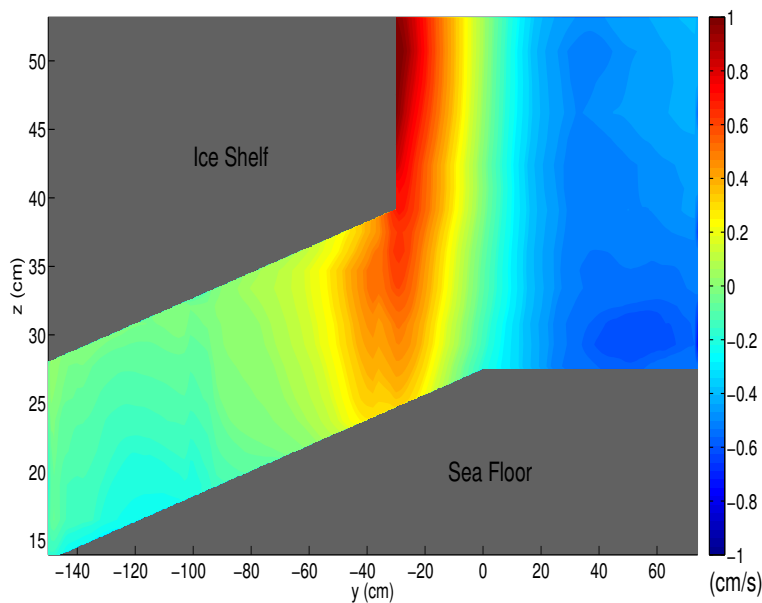


Fig. 7 The time-mean, x -mean zonal velocity on the z - y plane for the Control Run. A strong eastward jet can be seen moving along the ice front and a return westward flow is seen along the northern wall. There is very little zonal motion inside the ice shelf cavity.

587

588

589 3.2 Differences in the experimental runs:

590 While all the experimental runs had the features described in the section
 591 above, changing the ice shelf geometry and the flux of the dense and fresh wa-
 592 ter sources, caused significant differences in the behavior of the flow. Figure 9
 593 shows the vertically integrated meridional volume flux for the experiments in-
 594 volving different geometries. This figure highlights the sensitivity of the system
 595 to changes in buoyancy sources and ice shelf geometry. The main differences
 596 between the various experimental runs are pointed out in this section.

597

598 The results of Thickness Investigation: are shown in the top row of Fig. 9.
 599 Recall, the same Control Run was used for all three investigations, and is
 600 shown in the center of Fig. 9. The Little Gap Run, has almost no motion in-
 601 side the ice shelf cavity, and very little flux into the cavity through the dense
 602 boundary currents. Most of the motion in this run was confined to the con-
 603 tinental shelf. In contrast, in the Big Gap Run, we see that there is a larger

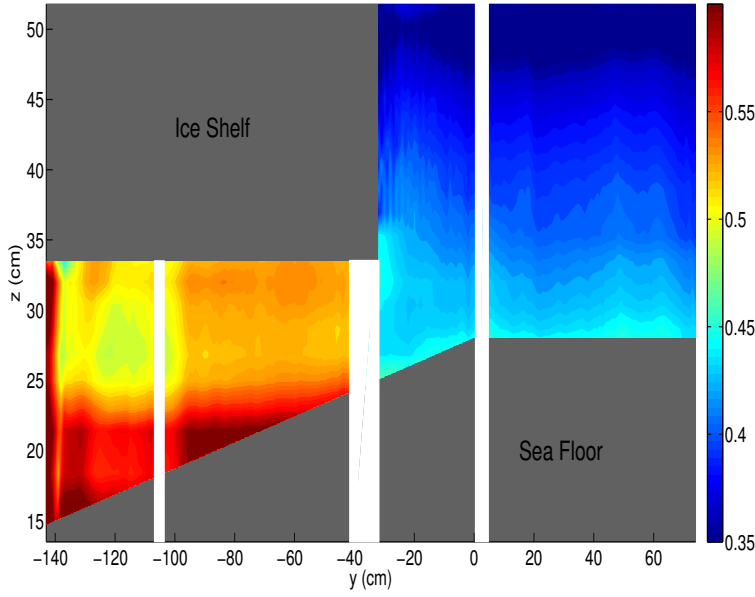


Fig. 8 The time-mean interior concentration field for The Stretch is shown at different latitudes. The interior concentration is defined as the average concentration between $x = 40$ and $x = 172$. In this figure we can see strong density gradient across the ice front.

flux of dense water into the cavity through the dense plume and more motion inside the ice shelf cavity. Furthermore, very little water is recirculated on the continental shelf along the ice front, meaning that the jet along the ice front is largely reduced, and the gyre offshore of the ice shelf disappears completely. The Control Case is an intermediate case which has some flux of water into the cavity, but still has a substantial jet running along the ice front.

The results from Gradient Investigation are shown in the second row in Fig. 9. The results of this investigation indicates that the gradient of the water column thickness in the ice shelf cavity has a strong influence on the circulation. The Stretch Run run is particularly noteworthy in that it has a lot of motion inside the ice shelf cavity. The gyre on the continental shelf in the Stretch Run is less strong. In contrast, the Pinch Run has relatively little movement inside the ice shelf cavity, but has a strong gyre on the continental shelf. The Control Run is again an intermediate case with some motion away from the boundary currents inside the ice shelf cavity and a reasonably strong gyre on the continental shelf.

We propose that the slope of the ice shelf controls the motion in the ice shelf cavity via the following mechanism: Fresh water is injected into the system vigorously by a distributed source at the grounding line. The injection of the

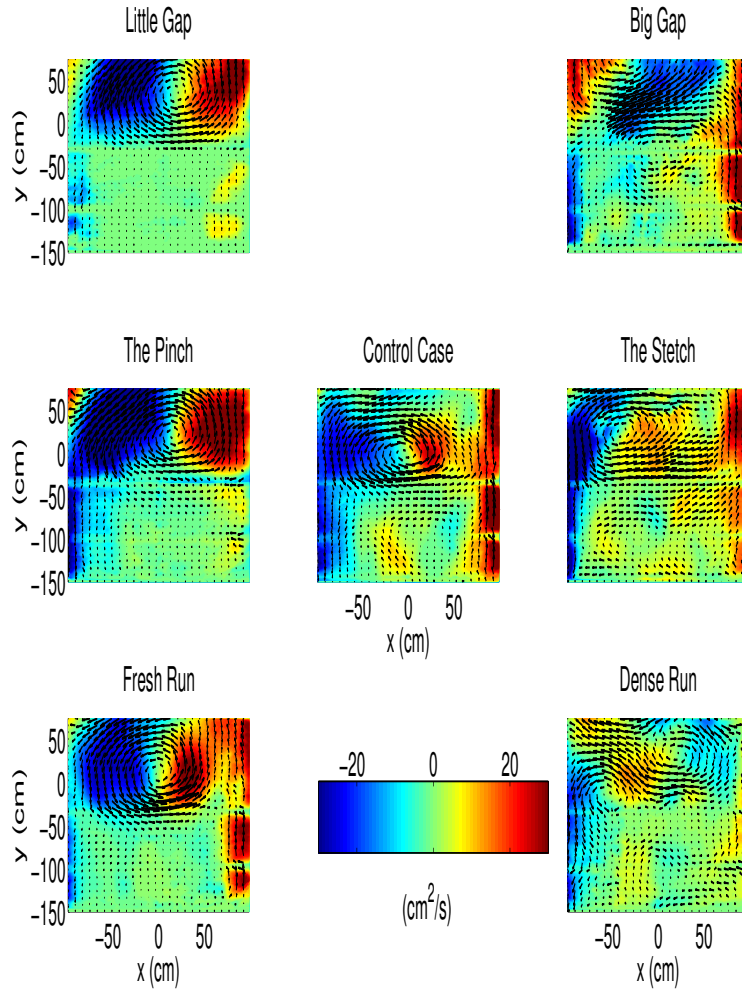


Fig. 9 The time-mean vertically integrated meridional volume flux for all the experimental runs. The arrows indicate direction and magnitude of the integrated volume horizontal flux. The figure shows how changing the geometry of the ice shelf and the dense and fresh sources has an effect significant on the circulation inside the ice shelf cavity. The three experimental runs in the column on the left of the figure all systematically show a more intense circulation on the continental shelf, and less intense cavity circulation, compared to the Control Run.

fresh water results in strong mixing near the fresh water source and causes the fluid columns near the fresh water source to largely barotropic. As a columns of fresh water drift northwards, the geometry of the ice shelf forces the column thickness to change, resulting in the production of vorticity. In the case of the Stretch Run, the fluid column thickness is decreased as a water column moves northwards, which generates negative vorticity. This acts in the same direction as the flow seen in the Control Run and increases the motion inside the cavity. In the Pinch Run, the fluid column thickness is increased when moving northwards. This generates positive vorticity which opposes the fluid motion seen inside the ice cavity in the Control Run, and suppresses motion inside the cavity.

The results of Buoyancy Investigation are shown in the bottom row of Fig. 9. The Fresh Run has a strong gyre on the continental shelf, but very little motion inside the ice shelf cavity. The Dense Run has a much smaller gyre on the continental shelf and has much more motion inside the ice shelf cavity. As expected, the fresh water plume is large in the Fresh Run, and small in the Dense Run, while the dense water plume is large in the Dense Run and small in the Fresh Run. The control case is an intermediate case with equally sized boundary currents, some motion inside the cavity, and a intermediate strength gyre on the continental shelf.

3.3 Shape of the dense plume

In this section we look more carefully at the structure of the dense plume for the different experimental runs. In Fig. 10 we plot the time-mean meridional velocity for each experimental run at $y = -54\text{cm}$, which is a latitude just inside the ice shelf cavity. The results are again positioned with Thickness Investigation shown in the top row, Gradient Investigation in the second row, and Buoyancy Investigation in the bottom row.

In almost all experimental runs the fastest moving and densest part of the plume is against the wall near the bottom. The velocity is seen to decay away from the wall toward the edge of the plume. The concentration (normalized density) contours have been plotted on top of Fig. 10. Figure 11 shows the time-mean concentration for the same slice of fluid. The concentration fields for the Control Run and the Dense Run are not plotted since there were problems with the calibrations. Comparing Fig. 10 and Fig. 11, one can see that the velocity contours lie parallel to the density contours in the densest part of the plume. The velocity contours of the plume take on a triangular shape near to the wall and then become more vertical as one moves away from the boundary. In all experimental runs, the zonal density gradient decreases away from the boundary. This results in a decrease in the vertical shear in merid-

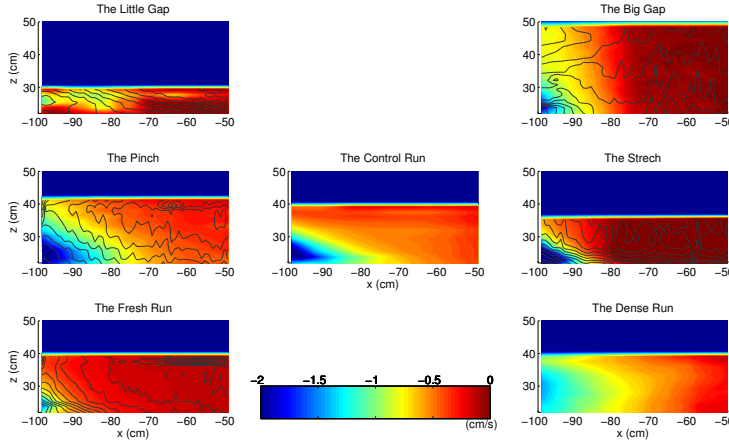


Fig. 10 The time-mean, meridional velocity (cm s^{-1}) of the dense plume at $y = -54\text{cm}$ is plotted for each experiment. Only the negative velocity has been plotted to allow the plume to be seen more clearly. Density contour lines have been plotted over the top.

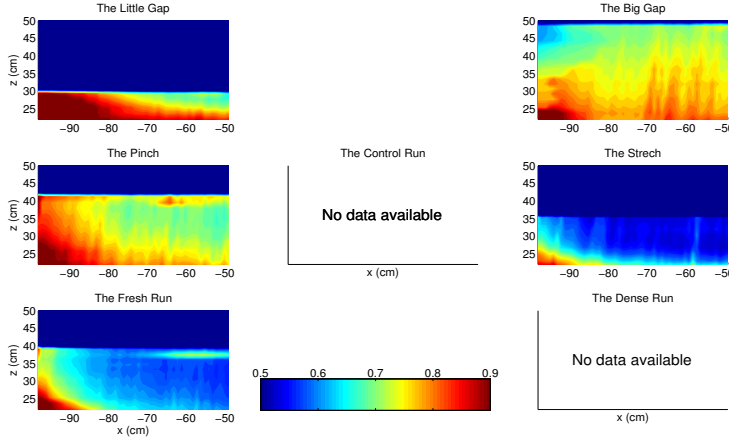


Fig. 11 The time-mean concentration contours of the dense plume at $y = -54\text{cm}$ is plotted for each experiment.

ional velocity as one moves away from the wall (see Fig. 10)

The structure of the dense plume is somewhat reminiscent of the observations of turbidity currents in submarine channels, which have an asymmetry in the heights of their levee banks [30] [8], or of the classic "cylinder collapse experiment" [38]. The densest water gets stacked against the wall which creates a

region of high pressure against the wall. The pressure gradient is balanced by the Coriolis force, which generates a southward velocity and the fluid moves down into the ice shelf cavity.

The results described in [8] emphasize the importance of Ekman layer dynamics in determining the transport of the gravity plumes in a turbidity current. Their experiments did not have an upper boundary. Never-the-less, their results suggest that the plumes found in our experiment and under an ice shelf, are likely to be affected by the upper boundary, which creates an upper Ekman layer.

In Fig. 12 the time varying volume flux through the dense plume is plotted. The volume flux is defined as:

$$\hat{V}(y) = - \int_A v(x, y, z) dx dz \quad (7)$$

A is the cross-sectional area of the plume. The cross sectional area of the plume is the area between the western wall and the plume edge. We define the edge of the dense plume using the following procedure: At each height we find the first 3 successive points closest to the western boundary which all have a meridional velocity $v > 0$. We define the first of these three points to be the edge of the plume and define our plume to be all points to the west of the plume edge. We allow for 3 points to make our calculation less susceptible to individual erroneous points.

Figures 10 and 11 show that the structure and size of the dense plume is affected by changes in the geometry of the ice shelf cavity and changes in the amount of dense and fresh water injected into the system. Figure 12 shows that the amount of water fluxed into the cavity through the dense plume is also sensitive to changes in these parameters.

The Thickness Investigation is shown in the top row of Figures 10, 11 and 12. These figures show that when the ice shelf cavity is thick there is a greater flux through the dense plume than for thinner ice shelf cavities. Southward moving water approaching the ice front is able to enter the ice shelf cavity more easily when the cavity thickness at the ice front is wider while for narrower cavity thicknesses some of this water is blocked by the ice shelf, and is forced to remain outside of the ice shelf cavity on the continental shelf. One could imagine that in the limiting case of a very wide cavity entrance, the flow entering the cavity would be unimpeded at the ice front, while for extremely narrow cavity thickness at the ice front, no water would be able to move into the cavity, and all water would recirculate on the continental shelf.

The Gradient Investigation, in the second row, shows that the Pinch Run has a larger flux through the dense plume than the Stretch Run, while the Control Run has an intermediate amount. This is explained by noting that

the thickness of ice shelf cavity at the ice front in The Stretch is smaller than the thickness of the ice shelf cavity at the ice front in The Pinch with the Control Run having an intermediate cavity thickness at the ice front. This result is consistent with Thickness Investigation.

The Buoyancy Investigation, in the third row, shows that if more dense water is injected into the system, it results in a larger plume flowing into the cavity (this can be seen in the velocity data in Fig. 10 and Fig. 12).

3.4 Plume variability

Most of the above analysis has focused on the time mean fields. However, when we look at the time dependent data, we see that the circulation inside the cavity and the flow through the plumes are in fact highly variable. In this section we focus on the time dependence of the flow in the dense plume. Movies showing the time evolution vorticity, kinetic energy and concentration fields throughout the cavity can be viewed online at <http://efdl.cims.nyu.edu/publications/refereed.html>.

Figure 12 shows a time series of the volume flux of the dense plume (defined above) at $y = -54$ (blue) and at $y = -110$ (green), which are both latitudes inside of the ice shelf cavity. A horizontal red line is plotted indicating the flux of water at the dense source in the experiment. The flux at the two latitudes vary together since the time scale of the oscillations is much longer than the time taken for fluid to move down the plume from the northern latitude to the southern latitude.

The most striking feature in Fig. 12 is that the various experimental runs have different volume fluxes through the dense plume, and that these volume fluxes are highly variable. The variabilities in the various experimental runs have different amplitudes and different periods depending on the geometry of the ice shelves and buoyancy sources used. As discussed in the previous section, the amplitude of volume flux through the plume is proportional to the thickness of the opening of the ice shelf cavity at the ice front.

In Thickness Investigation (top row of Fig. 12), we see that the plume is more variable for a thick ice shelf cavity than for the thin cavity. For the thick ice shelf, the amplitude of the variations is bigger, and the period of the variations is longer. The Control Run has an intermediate amount of variability. In Gradient Investigation (second row in Fig. 12), we see that period of the oscillations in the plume in the Stretch Run is larger than in the Pinch Run, with the Control Run having an intermediate period. The amplitude of the oscillations also appears to be larger in the Stretch Run. This is especially apparent when the time series are normalized. In the Buoyancy Investigation (bottom row of Fig. 12), we see that amplitude and period of the oscillations is

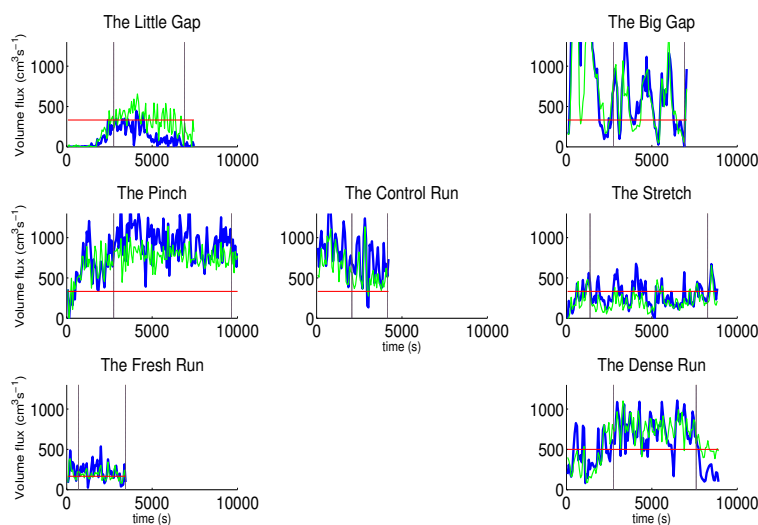


Fig. 12 Time series of the volume flux of the dense plume at $y = -54\text{cm}$ (blue) and at $y = -110$ (green), which are both latitudes inside of the ice shelf cavity. The horizontal axis shows time in seconds. A horizontal red line is plotted indicating the dense source flux rate in the experiment. The dashed vertical lines indicate the times between the time-averages were taken in the previous sections.

larger and longer for the Dense Run than for the Fresh Run with the Control Run being intermediate.

The variability of the plume seems to indicate how much the circulation inside the ice shelf cavity is influenced by the variability outside of the cavity. The experimental runs with strong dynamic barrier at the ice front, seem to restrict movement inside the ice shelf cavity, and to limit variability inside the plume. The runs which have a weaker dynamic barrier at the ice front have more motion inside the ice shelf cavity, and have a more variable dense plume.

Looking carefully at the time varying data, we see that the dense water does not move smoothly from the source to the plume, but instead arrives in pulses. These pulses cause the oscillations in the flow rate seen in Fig. 12. The fluid is injected smoothly into the domain by the dense source (i.e. without pulses), which implies that some other mechanism is causing the flow to be unsteady. The most likely candidates are baroclinic instability of the gyre on the continental shelf and that eddies are created at the dense source when the dense fluid was released into the domain.

4 Discussion

In the previous sections we saw evidence of the dynamic significance of the ice front in largely blocking water from entering and exiting the ice shelf cavity, and that this blocking effect was significantly altered by changing the ice geometry and buoyancy fluxes. We discuss these in turn:

The blocking effect of the ice shelf front has been noted by other authors using numerical models [11] [17]. Grosfeld (1997) [17] used a three dimensional numerical model and observed that the flow was dominated by the barotropic mode, which steers the flow along the ice front rather than into the ice shelf cavity. The presence of the ice shelf imposes a change in water column thickness which presents a barrier for the barotropic flow. The barotropic flow tends to move along $\frac{f}{H}$ contours which run parallel to the shelf. For this reason, the zonal jet outside the ice shelf cavity runs along the ice front but does not enter.

However, while the results presented above do demonstrate the blocking effect of the ice shelf, they also demonstrate that this blocking effect is not as severe as previously suggested [11] [17]. Figure 7 show that although the jet runs along the ice front, it does leak into the ice shelf cavity to some extent. There is a significant vertical shear in the velocity of the jet along the ice front. This indicates that the jet is not solely dominated by the barotropic mode. The leaking of the jet into the cavity may be a result of baroclinic instability. Furthermore, Fig. 5 shows there is some flux into and out of the ice shelf cavity away from the boundary currents, despite the dynamic barrier imposed by the ice shelf.

Furthermore, water is able to flux into and out of the cavity relatively freely through the dense and fresh plumes. This is because in the dense and fresh plumes, the stratification decouples the water column and the plumes are able to enter/exit the ice shelf cavity more easily [22].

The results from Thickness Investigation, Gradient Investigation and Buoyancy Investigation indicate that the blocking effect of the ice shelf front, the amount of movement inside the ice shelf cavity, and the flux of water through the density plumes, are strongly affected by the geometry of the ice shelf cavity, and the amount of dense and fresh water injected into the system. Figure 13 is a schematic which summarizes the findings discussed above. In Fig. 13, the dense plume, the circulation on the continental shelf and the circulation inside the ice shelf cavity are represented using arrows. The size of the arrows is an indication of the strength of the plumes and circulations observed in the experiment (not to scale). We use Figure 13 to summarize our results in terms of the non-dimensional parameters described in section 2.2.2.

The results in Thickness Investigation show that making the ice shelf cavity narrower (decreasing G_t), decreases the size of the dense plume, decreases

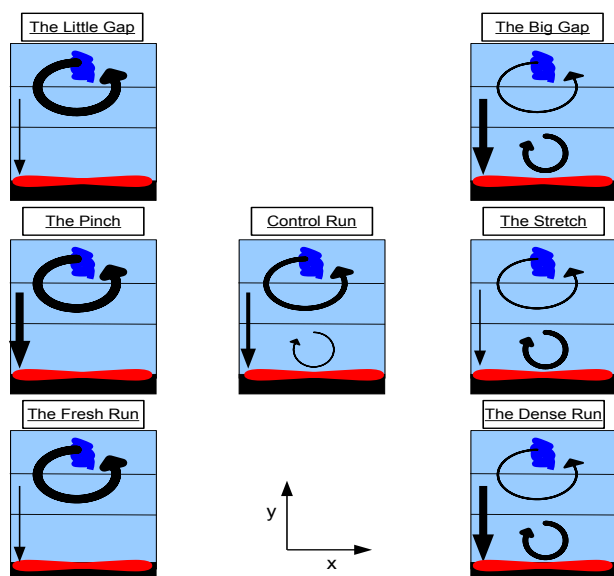


Fig. 13 A schematic summarizing the results from the three investigations. The size of the dense plume, the strength of the circulation inside the ice shelf cavity, and the strength of the circulation outside the ice shelf cavity are shown by the size of the arrows in each of the experimental runs (not to scale).

the circulation inside the ice shelf cavity, and increases the size of the gyre on the continental shelf outside of the ice shelf cavity. For larger values of G_t , the flux through the dense plume is increased, there is increased circulation inside the ice shelf cavity and there is a weaker gyre on the continental shelf. We conclude that the dynamic barrier at the ice front is strongest for small values of G_t . Small values of G_t decrease the connection between the water outside and inside the ice shelf cavity.

The Gradient Investigation shows the effect of changing the slope of the ice shelf. In this investigation we see the competing effects of local and global geometry conditions. Changes in G_t affect the ice front locally, while changes in G_s change the geometry on a larger scale. These competing effects allow the Stretch Run to have a small dense plume and yet also to have a lot of activity inside the ice shelf cavity and less activity outside the ice shelf cavity. The Pinch Run has a strong plume, and almost no motion inside the ice shelf cavity away from the boundary currents.

The strength of the flux through the dense plume is controlled locally by the parameter G_t . Decreased values of G_t result in a decreased flux through the dense plume. The Stretch Run, for example, has a narrower cavity thickness at the ice front, which means that a larger portion of the water approaching the ice front will be unable to enter the ice shelf cavity, and will have to remain

on the continental shelf. The Pinch Run has a wider cavity thickness at the ice front, which means that less of the water approaching the ice shelf cavity will be blocked from entering. The trajectory of the water approaching the ice shelf cavity is strongly influenced by the the cavity thickness at the ice front, and hence by the value of G_t . This result is the same as the result observed in the Thickness Investigation.

However, the results of the Gradient Investigation also indicate that the strength of the circulation inside the ice shelf cavity increases with decreasing values of G_s , despite the fact that the the values of G_t are decreasing too. This is the opposite of the result observed in the Thickness Investigation, where decreasing values of G_t resulted in decreasing circulation inside the ice shelf cavity. This shows that the circulation inside the ice shelf cavity is controlled more strongly by the gradient of the ice cavity thickness on the large scale, than the local thickness of the cavity at the ice front.

The movement inside the ice shelf cavity and the flux through the dense plume are both indications of the strength of the ice shelf as a dynamic barrier. The Gradient Investigation shows that the amount of motion inside the ice shelf cavity away from the plume, the strength of the circulation outside the ice shelf cavity and the blocking effect of the ice front away from the boundary currents, are controlled somewhat separately from the mechanism controlling the of the flux of water into the cavity through the dense plume.

The results from Buoyancy Investigation are much like the results in Thickness Investigation. For larger values of G_b , the dense plume is large, there is a lot of motion inside the ice shelf cavity, and there is not a lot of circulation on the continental shelf. For smaller values of G_b , the dense plume is small and there is much less communication between the water inside and outside the cavity. The Fresh Run has a strong circulation on the continental shelf, while there is very little motion inside the ice shelf cavity. We conclude that increasing the flux of dense water at the dense source (increasing G_b) has the effect of decreasing the dynamical barrier at the ice front which results in a stronger connection between the motion inside the ice shelf cavity and the motion on the continental shelf. Decreasing G_b results in a strengthening of the dynamical barrier at the ice front, and decreases the connection between the circulation inside of the ice shelf cavity and the circulation on the continental shelf.

5 Conclusion

A laboratory experiment has been set up to simulate the density-driven currents under ice shelves. The density current were forced by the input of dense

water on the continental shelf and fresh water at the grounding line. The central question asked was how water of different densities is able to enter and exit the ice shelf cavity and whether its ability to enter the ice shelf cavity is affected by the geometry of the ice shelf, and the strength of the dense and fresh water sources. This question has important scientific significance since the flux of dense water into the ice shelf cavity ultimately impacts the melt rates of the ice shelves.

From the results presented above, we draw three conclusions. Firstly, the results show that the movement in and out of the ice shelf cavity is largely restricted away from the boundary currents. In this sense the ice shelf front acts as a dynamical barrier restricting the connection between the water inside the ice shelf cavity and the water outside the ice shelf cavity. The dynamic barrier imposed by the ice front was observed to be present for various ice shelf geometries. However, the dynamical barrier was not as strong as previously argued [11] [17], and some water was able to pass through the ice front away from the boundary currents.

Our second finding was that fluid was able to enter and exit the ice shelf cavity very easily through the dense and fresh plumes running along the boundaries of the domain. These boundary currents take on a triangular shape with density contours lying parallel to velocity contours. The boundary currents transport water in and out of the ice shelf cavity very efficiently. This suggests that real world ice shelf cavity boundary currents are very efficient at transporting warm, salty water into the ice shelf cavity, and that warm, salty water arriving on the continental shelf will likely be fluxed into the cavity despite the dynamic barrier imposed at the ice shelf front.

The third finding is that changes to the ice shelf geometry and changes to the source strength of the dense and fresh water sources, was shown to have a significant effect on the time mean circulation under the ice shelf. The thickness of the ice shelf cavity at the ice front was shown to be an important parameter in setting the volume flux through the dense plume. The thickness of the ice shelf cavity, and the slope of the ice shelf were shown to have a strong influence on the strength of the circulation inside the ice shelf cavity. Ice shelves whose thickness decreases as one moves from the grounding line towards the ice front, were shown to have more motion inside the ice shelf cavity. Furthermore, it was shown that increasing the strength of the dense source resulted in an increase in the amount of motion inside the ice shelf cavity, and a weakening of the dynamical barrier imposed by the ice front.

The experiments described here are a first attempt at using laboratory experiments to mimic ice shelf circulation. We were able to simulate the circulation under the ice shelf and generate a flow with the same broad features as the circulation surmised under real-world ice shelves using limited data. The experimental results presented above show that the circulation inside the

ice shelf cavity, and the effectiveness of the ice front as a dynamical barrier, are both sensitive to the changes in the buoyancy sources and the ice shelf geometry.

References

1. ADRIAN R. J. (2005) Twenty years of particle image velocimetry. *Experiments in Fluids.*, **39**(2), 159-169.
2. M. rthun, Nicholls, K.W and Boehme, L. (2013): Wintertime Water Mass Modification near an Antarctic Ice Front. *J. Phys. Oceanogr.*, 43, 359365. doi: <http://dx.doi.org/10.1175/JPO-D-12-0186.1>
3. Assmann, K. , Hellmer, H. and Beckmann, A. (2003): Seasonal variation in circulation and water mass distribution on the Ross Sea continental shelf , **Antarctic Science**, **15** (1), pp. 3-11, doi: 10.1017/S0954102003001007
4. MACAYEAL D.R. (1984) Thermohaline Circulation Below the Ross Ice Shelf: A Consequence of Tidally Induced Vertical Mixing and Basal Melting. *J. Geophys. Res.*, **89**, 597-606.
5. MACAYEAL D.R. (1985) Evolution of Tidally Triggered Meltwater Plumes Below Ice Shelves, in *Oceanology of the Antarctic Continental Shelf* (ed S. S. Jacobs). *American Geophysical Union*, Washington, D. C.. doi: 10.1029/AR043p0133.
6. CENEDESE C., WHITEHEAD J. A., ASCARELLI T. A, OHIWA M. (2004) A dense current flowing down a sloping bottom in a rotating fluid. *J. Phys. Oceanogr.*, **34**, 188-203.
7. CONWAY, H., B. L. HALL, G. H. DENTON, A. M. GADES, AND E. D. WADDINGTON. (1999), Past and future grounding-line retreat of the West Antarctic ice sheet. *Science* 286, no. 5438 (1999): 280-283.
8. COSSU R., M. G. WELLS WHLIN A. K. (2004) Influence of the Coriolis force on the velocity structure of gravity currents in straight submarine channel systems. *J. Geophys. Res.*, **115**, C11016, doi:10.1029/2010JC006208..
9. ETLING D., GELHARDT F., SCHRADER U., BRENECKE F., KUHN G., CHABERT DHIERES G., DIDELLE H. (2000) Experiments with density currents on a sloping bottom in a rotating fluid. *Dynamics of Atmospheres and Oceans*, **31**, 139-164.
10. Davey, F. J. (2004), Ross Sea Bathymetry, in *Institute of Geological and Nuclear Sciences Geophysical Map 16*, scale 1:2,000,000, Version 1.0., Inst. of Geol. and Nucl. Sci., Lower Hutt, N. Z.
11. DETERMAN J., GERDES R. (1994) Melting and freezing beneath ice shelves: implications from a three-dimensional ocean-circulation model. *Ann. Glaciol.*, **20**, 413-419.
12. FOLDVIK A., GAMMELSRØD T., NYGAARD E., ØSTERHUS, S. (1983) Current measurements near Ronne Ice Shelf: Implications for circulation and melting. *J. Geophys. Res.* **106**, 4463-4477..
13. GORDON, A. L., ORSI, A. H., MUENCH, R., HUBER, B. A., ZAMBIANCHI, E., AND VISBECK, M., (2009), Western Ross Sea continental slope gravity currents, *Deep-Sea Res. Pt. II*, 56, 796817, 20 doi:10.1016/j.dsr2.2008.10.037.
14. GREENSPAN H.P., HOWARD L.N. (1963) On a time-dependent motion of a rotating fluid . *J. Fluid Mech.* **17**, 385.
15. GRIFFITHS, R.W. (1986) Gravity currents in rotating systems. *Ann. Rev. Fluid Mech.*, **18**, 59-89.
16. GRIFFITHS, R. W., HOPFINGER E. J. (1983) Gravity currents moving along a lateral boundary in a rotating frame. *J. Fluid Mech.* **134**, 357399..
17. GROSFELD K., GERDES R., DETERMAN J. (1997) thermohaline circulation and interaction between ice shelf cavities and the adjacent open ocean. *J. Phys. Oceanogr.*, **102**, C7, 15959-15610.
18. Hattermann T., Nøst A. K., Lilly J. M., Smedsrud J. M. (2012), Two years of oceanic observations below the Fimbul Ice Shelf, Antarctica. *Geophysical Research Letters*, 39, L12605: 16, doi:10.1029/2012GL051012.

19. HELLMER H.H., OLBERS D. J. (1989) A two-dimensional model for the thermohaline circulation under an ice shelf. *Antarctic Science*, **1**, 325- 336.
20. HOLLAND P. R., FELTHAM D. L. (2006) The effects of rotation and ice shelf topography on frazil-laden Ice Shelf Water plumes. *J. Phys. Oceanogr.*, **36**, 2312-2327.
21. HOLLAND D. M., JENKINS A. (1999) Modeling thermodynamic iceocean interactions at the base of an ice shelf. *J. Phys. Oceanogr.*, **29**, 1787-1800.
22. HOLLAND D. M., JENKINS A. (2001) Adaptation of an isopycnic coordinate ocean model for the study of circulation beneath ice shelves. *Mon. Wea. Rev.*, **129**, 1905-1927.
23. HOLMAN, J. P. (2002). HEAT TRANSFER. MCGRAW-HILL. P. 207.
24. HOLLAND P. R., JENKINS A., HOLLAND D. M (2008) The response of ice shelf basal melting to variations in ocean temperature. *J. Climate*, **15**, 2558-2572.
25. HOUCINE I., VIVIER J. M., PLASARI J. M., VILLERMAUX J. M. (1996) Planar laser induced fluorescence technique for measurements of concentration fields in continuous stirred tank reactors. *Exp. Fluids*, **22**, 95-10.
26. JENKINS, A. (1991) A one-dimensional model of ice shelf-ocean interaction. *J. Geophys. Res. -Oceans*, **96**, C11, 20671-20677.
27. JACOBS, S. S., HELLMER, H. H., JENKINS A. (1996) Antarctic ice sheet melting in the Southeast Pacific. *Geophys. Res. Lett.*, **23**, 957960..
28. JENKINS A., DUTRIEUX P., JACOBS S., MCPHAIL S., PERRETT J., WEBB A., WHITE D. (2012) Autonomous underwater vehicle exploration of the ocean cavity beneath an Antarctic ice shelf. *Oceanography* 25(3):202203, <http://dx.doi.org/10.5670/oceanog.2012.95>.
29. KILLWORTH O.D., PALDOR N., STERN M.E. (1984) Wave propagation and growth on a surface front in a two-layer geostrophic current. *J. Marine Res.*, **42**, 761-785.
30. KOMAR, P. D. (1969) The channelized flow of turbidity currents with application to Monterey deep?sea fan channel. *J. Geophys. Res.*, **74**, 4544-4558, doi:10.1029/JC074i018p04544.
31. G. LANE-SERFF, BAINES, P. (1998) Eddy formation by dense flows on slopes in a rotating fluid. *J. Fluid Mech*, **363**, pp. 229-252.
32. LEWIS E.L., PERKIN R.G. (1986) Ice pumps and their rates. *J. of Geophys. Res.*, **91**, 11756-11762.
33. MAKINSON K., SCHRÖDER M., ØSTERHUS S. (2005) Seasonal stratification and tidal current profiles along Ronne Ice Front. *Frisp Report*, **16**.
34. Makinson K., Schröder M., Østerhus S. (2006), Effect of critical latitude and seasonal stratification on tidal current profiles along Ronne Ice Front, Antarctica, *J. Geophys. Res.*, **111**, C03022, doi:10.1029/2005JC003062.
35. MAKINSON K., HOLLAND P.R., JENKINS A., NICHOLLS K.W., HOLLAND D.M. (2011) Influence of tides on melting and freezing beneath Filchner-Ronne Ice Shelf, Antarctica. *Geophys. Res. Letters*, **113**, C08043.
36. MATHIOT P., JOURDAIN N.C., BARNIER B., GALLE B., MOLINES J.M., LE SOMMER J., PENDUFF T. (2012) Sensitivity of coastal polynyas and high-salinity shelf water production in the Ross Sea, Antarctica, to the atmospheric forcing. *Ocean Dynamics* 62:701723 DOI 10.1007/s10236-012-0531-y
37. MILLERO F. J. (1986) Freezing point of sea water: Eighth report of the Joint Panel of Oceanographic Tables and Standards. *Appendix 6, UNESCO Tech. Pap. Mar. Sci.*, **28**, 2931.
38. MARSHALL J., PLUMB R.A. (2008) Atmosphere, Ocean and Climate Dynamics. *page* **123 -128**.
39. NICHOLLS K.W. (1996) Temperature variability beneath Ronne Ice Shelf, Antarctica, from thermistor cables. *J. Phys. Oceanogr.*, **11**, 1199-1210.
40. NICHOLLS K.W., ØSTERHUS S., MAKINSON K., GAMMELSRØD T., FAHRBACH E. (2009) Ice-Ocean processes over the continental shelf of the southern Weddell Sea, Antarctica: A review. *Rev. Geophys.*, **47**, RG3003, doi:10.1029/2007RG000250..
41. NICHOLLS K. W., PADMAN L., SCHRÖDER M., WOODGATE R. A., JENKINS A., ØSTERHUS S. (2003) Water mass modification over the continental shelf north of Ronne Ice Shelf, Antarctica, *J. Geophys. Res.*, **108**(C8), 3260, doi:10.1029/2002JC001713.
42. ORSI, A. H., W. M. SMETHIE JR., AND J. L. BULLISTER, (2002) On the total input of Antarctic waters to the deep ocean: A preliminary estimate from chlorofluorocarbon measurements, *J. Geophys. Res.*, **107**(C8), doi:10.1029/2001JC000976.

-
- 1046 43. NUNEZ-RIBONI I., FAHRBACH E. (2010) An observation of the banded structure of the
1047 Antarctic Coastal Current at the prime meridian. *Polar Res.* **29**, 322-329.
- 1048 44. RIGNOT E., JACOBS S. (2002) Rapid bottom melting widespread near Antarctic Ice
1049 Sheet grounding lines. *Science*, **296**, 2020-2023.
- 1050 45. STERN M.E., WHITEHEAD J.A., HUA, B.L. (1982) The intrusion of a density current
1051 along the coast of a rotating fluid. *J. Fluid Mech.* **123**, 237-266.
- 1052 46. A.A. Stern, M.S. Dinniman, V. Zagorodnov, S.W. Tyler, and D.M. Holland1, Intrusion
1053 of warm surface water beneath the McMurdo Ice Shelf, Antarctica (2013), Intrusion of
1054 warm surface water beneath the McMurdo Ice Shelf, Antarctica, *J. of Geophys. Res.*
- 1055 47. WAHLIN A.K., DARELIUS E., CENEDESE C., LANE-SERFF G.F. (2008). LABORA-
1056 TORY OBSERVATIONS OF ENHANCED ENTRAINMENT IN DENSE OVERFLOWS IN THE PRES-
1057 ENCE OF SUBMARINE CANYONS AND RIDGES. *Deep-sea Research 1*, **55**, 737-750. DOI:
1058 10.1016/J.DSR.2008.02.007.
- 1059 48. WELLS M.G., WETTLAUER J. S. (2008). THE CIRCULATION IN LAKE VOSTOK: A LAB-
1060 ORATORY ANALOGUE STUDY. GEOPHYSICAL RESEARCH LETTERS. 35, L0350, DOI:10.1029
- 1061 49. ZATSEPIN A.G., DIDKOVSKI V.L., SEMENOV A.V. (1996) A self-oscillatory mechanism
1062 of inducing a vortex sloping bottom in a rotating fluid. *Oceanology* **38**, 4350.